Available online at www.sciencedirect.com

ScienceDirect

Journal of the European Ceramic Society 31 (2011) 2285–2294

www.elsevier.com/locate/jeurceramsoc

Thermal aging behavior of plasma sprayed $LaMgAl_{11}O_{19}$ thermal barrier coating

Xiaolong Chen[a,b], Yu Zhao[a,b], Wenzhi Huang[a,b], Hongmei Ma[a], Binglin Zou[a], Ying Wang[a], Xueqiang Cao[a,*]

[a] *State Key Laboratory of Rare Earth Resources Utilization, Changchun Institute of Applied Chemistry, Chinese Academy of Sciences, Changchun 130022, China*

[b] *Graduate School of the Chinese Academy of Sciences, Beijing 100049, China*

Received 5 January 2011; received in revised form 16 May 2011; accepted 25 May 2011

Abstract

The crystallization behavior of the amorphous phase of the plasma sprayed $LaMgAl_{11}O_{19}$ (LaMA) coating during thermal aging processes has been investigated. Results indicate that LaMA coating exhibits much similar microstructure and thermal properties such as close coefficient of thermal expansion and specific heat capacity etc. to the sintered LaMA bulk after aging at 1673 K for 20 h. On the other hand, a solid state reaction seems to occur to reform the ideal magnetoplumbite-type LaMA phase coupled with the formations of the La-rich aluminate intermediate phases. When the aging temperature is held between 1273 K and 1473 K, nanosized platelet-like grains as well as sub-grains with high aspect ratios are present. The phase stability has been investigated through the chemical compositions and X-ray diffraction analysis. The recrystallization mechanism of the amorphous LaMA coating has been explored by tracing the microstructure evolutions during thermal aging process.

Keywords: B. Platelets; B. Microstructure-final; C. Thermal properties; C. Thermal expansion; Thermal barrier coatings

1. Introduction

Ceramic thermal barrier coatings (TBCs) are playing increasingly important roles in modern industry, which are frequently engineered for thermal, corrosion and erosion protections of the hot-section components in gas turbine and diesel engine systems in order to realize the growing demands for improved engine efficiency and durability.[1–6] A typical TBC system usually presents the duplex layer structure consisting of a metallic bond coat (MCrAlY, M = Ni and Co) as the oxidation-resistant layer followed by a thermal insulation ceramic top coat deposited either by electron beam-physical vapor deposition (EB-PVD) or atmospheric plasma spraying (APS). During the past decades, 6–8 wt.% yttria partially stabilized zirconia (YSZ) with outstanding thermomechanical properties in service has been widely used as the TBC material. However, at the operating temperature above 1200 °C, YSZ coating usually suffers serious sintering, phase transformation from the initial non-transformable tetragonal (t') zirconia to the final monoclinic (m) zirconia accompanied by a 4–6% volume expansion, which would cause spallation failure of the ceramic coating and finally limit its further applications. As a result, some other metal oxides such as CeO_2, Sc_2O_3, In_2O_3, Ta_2O_5 and Re_2O_3 (Re = La, Nd, Sm, Gd, Dy and Yb) doped ZrO_2 counterparts have been developed for various purposes of enhancing the phase stability or the corrosion resistances.[7–13] On the other hand, new TBC candidate materials such as the pyrochlore-type rare earth zirconates ($Re_2Zr_2O_7$, Re = La, Nd, Sm and Gd) with low thermal conductivity, high phase stability and moderate coefficient of thermal expansion (CTE),[3,14–18] the fluorite-type $Re_2Ce_2O_7$ (Re = La and Nd),[19,20] and the perovskite-type $SrZrO_3$[21] have also been proposed and extensively studied for potential applications.

Recently, much effort has been devoted to evaluating another class of oxides with the magnetoplumbite-type structure as new TBC candidate materials. Such kind of oxides usually crystallize in hexagonal platelet-like grains and exhibit outstanding sintering resistance and high temperature phase stability.[22–25] Wherein, $LaMgAl_{11}O_{19}$ (LaMA) is the first one that has been widely studied.[26–30] Besides, as reported in previous works,[31,32] LaMA single layered coating is the only one that exhibits a close

---

[*] Corresponding author. Tel.: +86 431 85262285; fax: +86 431 85262285.
E-mail address: xcao@ciac.jl.cn (X. Cao).

0955-2219/$ – see front matter © 2011 Elsevier Ltd. All rights reserved.
doi:10.1016/j.jeurceramsoc.2011.05.036

thermal cycling lifetime to the traditional YSZ coating at the similar testing conditions. However, LaMA as a new TBC candidate material also has some obvious shortcomings, such as: (1) the EB-PVD LaMA coating, usually characterized by the columnar structure with superior strain tolerance and service lifetime, has not been successfully prepared up to now[33] and (2) for a plasma sprayed LaMA coating, partial decomposition of LaMA oxide usually occurs and a large amount of amorphous phase also presents due to the rapid quenching from the molten state.[25,26,32] The following recrystallization of the coating during high temperature service may put questions on the reliability of the LaMA coating.

In such a case, the thermal aging behavior of plasma sprayed LaMA coating has been investigated in order to better understand its recrystallization mechanism and as well as the tightly correlated microstructure evolutions, phase stability and thermomechanical properties.

2. Experimental procedures

LaMA powders were synthesized by a solid state reaction method. La_2O_3 (99.99%, Guangdong Chenghai Chemicals Co., Ltd.), γ-Al_2O_3 (99.99%, Tangshan Huatai Functional Ceramic Materials Co., Ltd.) and MgO (99.2%, Wuzi Zehui Chemicals Co., Ltd.) were selected as the starting materials. The three powders in proper ratio were ball-milled by zirconia milling balls and were heated at 1923 K for 24 h to obtain the final product. The as-synthesized LaMA powders mixed with arabic gum and deionized water were subjected to ball-mill mixing again and were later spray-dried (Jiangsu Yangguang Ganzao Co., Ltd.). The obtained free-flowing LaMA powders with the particle size of 20–120 μm were sieved for plasma spraying. The spray-dried powders were plasma sprayed onto a graphite substrate using the Sulzer Metco plasma spraying unit with a F4-MB gun to produce a LaMA coating with a thickness of ∼1.2 mm.

After removing from the graphite substrate, the freestanding as-sprayed LaMA coating was cut into bars with dimensions of 1.5 cm × 1.5 cm × 1.2 mm. These bars were isothermally aged in a muffle furnace at 873 K, 1073 K, 1173 K, 1273 K, 1473 K, and 1673 K for 20 h, respectively. The isothermally aged samples together with the as-sprayed sample were examined by X-ray diffraction (XRD, Bruker D8 Advance diffractometer, Cu-Kα radiation, $\lambda = 0.15406$ nm) in the range of $2\theta = 15$–$80°$, with a step size of 0.02° and a counting time of 0.5 s per step. X-ray fluorescence spectrometer (XRF, PANalytical PW-2403 apparatus) was employed to determine the chemical compositions of the as-synthesized LaMA powder and the as-sprayed LaMA coating. The fractured cross-sections of all samples were observed by scanning electron microscope (SEM, XL-30 FEG, Philips). High-resolution transmission electron microscopy examination (HR-TEM, Tecnai F20) was performed on the LaMA coating before (as-sprayed condition) and after thermal aging at 1673 K for 20 h. The fine particles used for TEM examinations were obtained by grinding thin slices of LaMA coating. Vickers microhardness measurements were performed on the polished cross-sections of the coatings with a load of 300 g and a dwell time of 15 s (FM-700, Future-Tech, Japan). About 20 measurements were taken for each specimen. The coating samples before and after thermal aging at 1673 K for 20 h with the dimensions of 25 mm × 4 mm × 1 mm were selected for thermal expansion measurements. The CTEs of the coatings were determined between 308 and 1673 K using the Netzsch 402C high-temperature dilatometer. Thermogravimetric analysis (TGA) and differential scanning calorimetry (DSC) analysis were also performed from room temperature (RT) to 1673 K at a heating rate of 10 K min^{-1} in N_2 atmosphere using a Netzsch STA 449 F3 Jupiter simultaneous thermal analyzer. The specific heat capacity of the sample was calculated relatively to the specific heat capacity of the sapphire reference sample, and three consequent tests were performed for each sample. The weight of the sample prior to DSC tests was about 40 mg and it was ultrasonically cleaned and dried before testing.

3. Results and discussion

3.1. Debye temperature and heat capacity

LaMA with the magnetoplumbite-type structure has been widely used as laser and luminescent materials, catalyst supports and catalysts for high temperature catalytic combustion, as well as used for the immobilization of nuclear waste[34–36] and TBC candidate material. Presently, as an important parameter of such a solid material, the Debye characteristic temperature (θ_D) of LaMA has been calculated from two important experimental elastic properties such as Young's modulus and Poisson's ratio whose values have recently been reported by Jiang et al.[37] As is well known, θ_D is proportional to the mean Debye sound velocity (v_m) of a solid by the following equation[38]:

$$\theta_D = \frac{h}{k_B}\left[\frac{3n}{4\pi}\left(\frac{N_A\rho}{M}\right)\right]^{1/3} v_m \tag{1}$$

where h and k_B are Planck's and Boltzmann's constants, respectively. N_A is Avogadro's number, ρ is the density, M is the molecular weight of the solid, and n is the number of atoms in the molecule (here, $n = 32$ for $LaMgAl_{11}O_{19}$). The mean sound velocity can be determined as[39]:

$$v_m = \left[\frac{3(v_s v_l)^3}{2v_l^3 + v_s^3}\right]^{1/3} \tag{2}$$

where v_l and v_s are longitudinal and shear sound velocities, respectively, which can be calculated from the bulk modulus B and shear modulus G according to the equations as[39]:

$$v_l = \left(\frac{B + (4G/3)}{\rho}\right)^{1/2}, \quad v_s = \left(\frac{G}{\rho}\right)^{1/2} \tag{3}$$

Based on the reported values of the Young's modulus (E) and the Poisson's ratio (υ),[37] presently, the bulk modulus B and shear modulus G can be calculated from the well-known relationships:

$$B = \frac{E}{3(1-2\upsilon)}, \quad G = \frac{E}{2(1+\upsilon)} \tag{4}$$

The calculated values are listed in Table 1. The Debye characteristic temperature calculated from the elastic proper-

Table 1
The theoretical density, mechanical constants (Poisson's ratio, Young's, Bulk and Shear modulus, υ, E, B, G) and the longitudinal, shear, and mean sound velocities (ν_l, ν_s, ν_m), and the Debye temperature θ_D of the $LaMgAl_{11}O_{19}$ (the values of υ and E are after Ref. 37).

Material	ρ (g/cm^3)	υ	E (GPa)	B (GPa)	G (GPa)	ν_s (m/s)	ν_l (m/s)	ν_m (m/s)	θ_D (K)
$LaMgAl_{11}O_{19}$	4.285	0.23	295	182	120	5292	8934	5861	832

ties of LaMA is 832 K. Debye characteristic temperature is an essential characteristic structure parameter of a solid, which is directly related to the binding force among atoms comprising the materials.[40] It is an important physical quantity to characterize the material properties such as the thermal vibration of atoms and phase transitions etc. For LaMA oxide as a new TBC candidate material, Debye characteristic temperature is an important parameter responsible for the temperature dependent factor of the thermal conductivity.

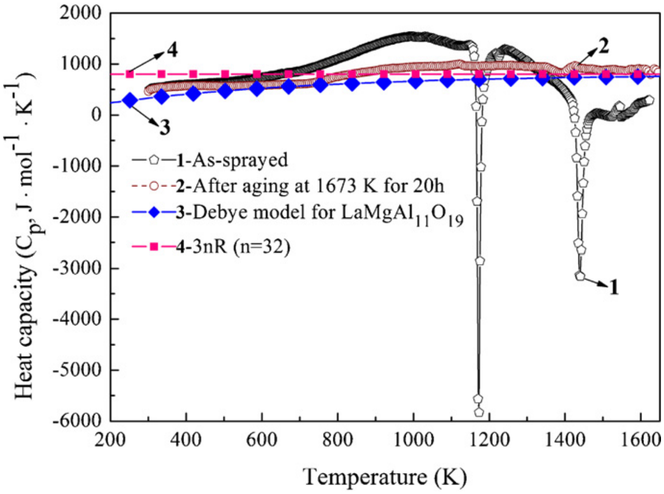

Fig. 1. Measured heat capacities (C_p) of the LaMA coating before and after aging at 1673 K for 20 h, as well as the theoretical C_p of LaMA oxide obtained from the Debye model.

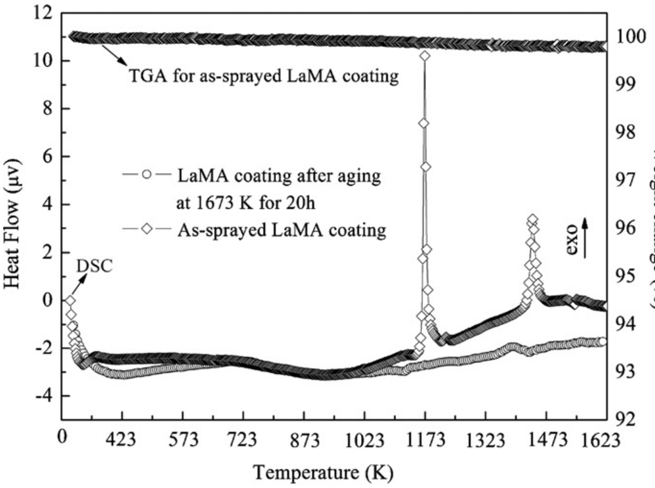

Fig. 2. Comparison of the DSC curves of the LaMA coating before and after aging at 1673 K for 20 h, as well as the TGA curve of the as-sprayed LaMA coating versus temperature.

As reported in previous works,[26,27] plasma sprayed LaMA coating like the well known mullite coating usually produces a structure consisting of a large amount of amorphous phase, and it is inevitable that recrystallization of the amorphous phase will occur during the following high temperature service. In order to further understand the phase transition behavior of plasma sprayed LaMA coating, the temperature dependence of heat capacities of the LaMA coating before and after aging at 1673 K for 20 h has been determined for the purpose of comparison. As shown in Fig. 1, the molar specific heat capacity of the as-sprayed LaMA coating increases across the temperature range of 303–995 K. Further, it suffers two sharp decreases around 1172 K and 1440 K, respectively. The sudden changes in C_p values are believed to be caused by the discrete change of the heat resulted from the phase transitions of the as-sprayed LaMA coating during heating. Furthermore, corresponding to the collected TG–DSC curves of the as-sprayed LaMA coating as illustrated in Fig. 2, no sudden mass changes occur around 1172 K and 1440 K where two sharp exothermal peaks appear. The TG–DSC analysis confirms that only phase transitions take place around such two temperature points instead of the oxidation or volatilization of LaMA coating which would lead to mass increase or loss. However, the specific heat capacity of the thermally aged LaMA coating shows no sudden changes, and the exothermal peaks also disappear as shown in the DSC curve in Fig. 2. These results display that phase transitions of the as-sprayed LaMA coating have been finished after aging at 1673 K for 20 h. Previous studies have pointed out that the first sharp exothermal peak around 1172 K is caused by the recrystallization of the amorphous component of the as-sprayed LaMA coating, while the second one is ascribed to the γ to α-Al_2O_3 phase transition.[26] It's easy to note that the recrystallization behavior and phase transition are irreversible once the more stable phases have formed. The molar specific heat capacity of the thermally aged LaMA coating is temperature dependent from room temperature (RT) to about 800 K as illustrated in Fig. 1. Then it seems to approach to an asymptotic value at a higher temperature. As predicted by the law of Dulong–Petit, when the temperature exceeds the Debye characteristic temperature, the specific heat of one atom is close to a constant of $C_p \rightarrow 3N_A k_B$ ($\sim$25 J K^{-1} mol^{-1}). For $LaMgAl_{11}O_{19}$, as the patterns shown in Fig. 1, the calculated Dulong–Petit value is about 800 J K^{-1} mol^{-1}, such a theoretical value is only slightly lower than the measured value of the LaMA coating after aging at 1673 K. This means that the as-sprayed LaMA coating will exhibit the same thermal properties to the corresponding LaMA bulk after a high temperature aging. Besides, as can be seen in Fig. 1, the as-sprayed LaMA coating exhibits a higher C_p value than its aged counterpart from RT to about 1300 K. It is believed that the presence of the amorphous phases with the structural disorder and a weaker interatomic coupling result in the as-sprayed LaMA coating a relative higher C_p

value consequently. For comparison, the theoretical lattice specific heat capacity (C_D) of the $LaMgAl_{11}O_{19}$ has been calculated according to the well-known Debye model:

$$C_D = 9nR\left(\frac{T}{\theta_D}\right)^3 \int_0^{\theta_D/T} \frac{x^4 e^x}{(e^x - 1)^2} dx \tag{5}$$

As the theoretical heat capacity (C_D) curve shown in Fig. 1, it displays a good conformity to the variation trend of the measured values of the LaMA coating after aging at 1673 K for 20 h. C_p is an important parameter that appears in the thermal conductivity of LaMA oxide which finally influences the performance of the LaMA coating in high temperature service. The extremely sharp decreases in C_p values resulted from the recrystallization and phase transitions of the as-sprayed LaMA upon heating may cause sharp changes in thermal insulating efficiency, resulting in the formations of residual thermal stresses and a reduced thermal shock resistance of a TBC system with an as-sprayed LaMA top coat. Therefore, the subsequent heat treatment of an as-sprayed LaMA coating seems to be preferable to overcome these problems in order to make the quality of the LaMA coating more reliable.

3.2. *Phase analysis*

XRD analysis has been performed on the LaMA coating before and after isothermal aging at different temperature for 20 h to trace the phase transition behavior, and the results are shown in Fig. 3. XRD patterns of the as-sprayed LaMA coating illustrated in Fig. 3(a) indicates the presence of the amorphous phase denoted by a broad hump at 2θ range about 26–34°, and as well as the crystalline LaMA phase whose characteristic peaks can be identified. Besides, some weak peaks ascribed to $LaAlO_3$ and unidentified phases are also present. When we enhance the thermal aging temperature from 873 K to 1273 K, as depicted by the XRD patterns in Fig. 3(b)–(e), the XRD peaks gradually get sharper, and the broad hump at the 2θ range about 26–34° gradually flattens, indicating that a higher aging temperature will lead to a better crystalline condition for all the phases presenting in the LaMA coating including the pure LaMA phase as well as other secondary phases. With the enhancement in aging temperature, it is found that the typical characteristic peaks ascribed to the unidentified phase sharpen remarkably, α-Al_2O_3 peak and another more obvious characteristic peak of the $LaAlO_3$ phase at $2\theta = 33.3°$ appear. However, as the XRD patterns shown in Fig. 3(f), it is very interesting to find that $LaAlO_3$ phase peaks seem to disappear after aging at 1473 K for 20 h. Fig. 3(g) shows the XRD patterns of the LaMA coating after aging at 1673 K, it is very unusual to observe the $MgAl_2O_4$ spinel peaks, and the $LaAlO_3$ characteristic peaks are still absent. Besides, the relative intensity of one unidentified peak at $2\theta = 30.1°$ significantly decreases and a new unidentified peak as marked in blue at $2\theta = 28.5°$ appears in comparison with the XRD patterns shown in Fig. 3(b)–(f).

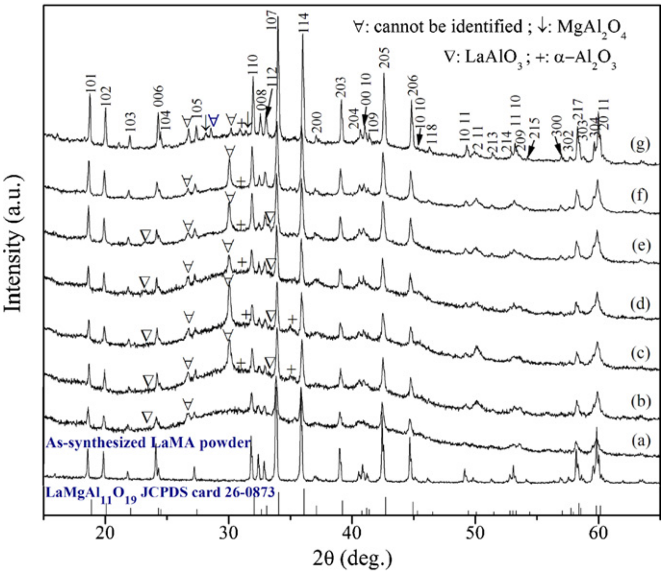

Fig. 3. XRD patterns of the as-synthesized LaMA powder through a solid state reaction method and LaMA coatings: (a) as-sprayed, and after aging at (b) 873 K, (c) 1073 K, (d) 1173 K, (e) 1273 K, (f) 1473 K and (g) 1673 K for 20 h, respectively.

In order to better understand the special phenomenon appearing in the results of the XRD analysis as shown in Fig. 3(f) and (g), the chemical compositions of the as-synthesized LaMA powder and the as-sprayed LaMA coating were determined by XRF, and the results are listed in Table 2. Compared with the theoretical value, the chemical composition of the as-synthesized LaMA powder seems to have deviated to nonstoichiometry ratio by obvious losses of Al_2O_3 and MgO. During ball-milling process, MgO and especially for γ-Al_2O_3 accounting for relative larger volume percents among such a La_2O_3–MgO–Al_2O_3 ternary system may suffer more serious losses, resulting in the final deviation in stoichiometry ratio. For the as-sprayed LaMA coating, the contents of the Mg and Al elements show further decreases, which are believed to be caused by the partially melting and volatilization of LaMA oxide when the powders passed through the plasma flame with an extremely high temperature. On the other hand, as reported in previous works,[24,27] the heterogeneities in the phase sequences of the LaMA coatings might occur during the plasma spraying process which would cause some contributions to the deviation of the chemical composition to some extent. As the measured chemical compositions shown in Table 2, the molar ratios of La_2O_3–MgO–Al_2O_3 to form the ideal magnetoplumbite-type LaMA phase with a strict stoichiometry ratio are $0.375(La_2O_3)\cdot 0.75MgO\cdot 4.125(Al_2O_3)$ and $0.345(La_2O_3)\cdot 0.69MgO\cdot 3.975(Al_2O_3)$ for the as-synthesized LaMA powder and as-sprayed LaMA coating, respectively. Therefore, excessive La_2O_3 and Al_2O_3 are present. As pointed out by Gadow et al.,[30] the presence of redundant La_2O_3 and MgO would result in the formations of a multiphase region including $LaMgAl_{11}O_{19}$, $MgAl_2O_4$, $LaAlO_3$, and MgO etc. As a result, in the present study, the weak peaks of $LaAlO_3$ phase which is a La-rich phase compared with the LaMA oxide, often present in the XRD patterns of the as-sprayed LaMA coating and as well as the as-synthesized LaMA powder, though it can not be obviously detected due to its low content as shown in Fig. 3. Thereby, the presence of α-Al_2O_3 phase in the LaMA coating after aging at the temperatures below 1173 K as shown in Fig. 3 is

Table 2
Chemical compositions of the as-prepared LaMA powder and coating.

Material	La (wt.%)	Mg (wt.%)	Al (wt.%)	Chemical formula
Ideal $LaMgAl_{11}O_{19}$	18.18	3.18	38.85	$0.5(La_2O_3)\cdot MgO\cdot 5.5(Al_2O_3)$
As-synthesized powder	22.08	2.86	36.57	$0.5(La_2O_3)\cdot 0.75MgO\cdot 4.29(Al_2O_3)$
As-sprayed coating	22.77	2.76	36.20	$0.5(La_2O_3)\cdot 0.69MgO\cdot 4.11(Al_2O_3)$

likely an indication of the partial decomposition of LaMA oxide during plasma spraying process which can be expressed by the following equation as pointed out in our previous works[32,41]:

$$LaMgAl_{11}O_{19} \rightarrow LaAlO_3 + MgO + 5Al_2O_3 \tag{6}$$

With gradual enhancement in aging temperature, there occurs an increase in the peak intensities of the secondary phases such as the Al_2O_3, $LaAlO_3$ and the unidentified phase. As the phase diagram of ternary system La_2O_3–MgO–Al_2O_3 shown in Fig. 4, for such an established system, the magnetoplumbite phase forms in a narrowly restricted composition, usually follows the formula La_2O_3–xMgO–$y$$Al_2O_3$, where $0.2 \leqq x \leqq 3.3$, $10.0 \leqq y \leqq 13$, and with the ideal composition of La_2O_3–2MgO–$11Al_2O_3$ ($2LaMgAl_{11}O_{19}$, $x = 2$ and $y = 11$).[30] Such information indicates that a slight deviation in stoichiometry ratio is allowed to some extent to form the magnetoplumbite-type LaMA phase in such a La_2O_3–MgO–Al_2O_3 ternary system. This tolerance deviation in stocihiometry ratio may be one of the reasons that all the XRD patterns of the LaMA coating and as-synthesized powders shown in Fig. 3 exhibit rather limited impurity phases though superfluous La_2O_3 and Al_2O_3 have already led to a nonstoichiometry ratio. Therefore, on one hand, when LaMA coating is isothermally aged at 1473 K, a slow solid state reaction to further form the magnetoplumbite-type La–Mg–Al phase is going to occur, thus giving rise to the absence of $LaAlO_3$ phase. On the other hand, the phase diagram shown in Fig. 4 reveals the presences of the La-rich phases such as $LaMg_{0.12}Al_{0.88}O_{2.94}$, $La_4MgAl_2O_{10}$ and $La_3MgAl_2O_7$ etc. Hence, $LaAlO_3$ as an intermediate phase may transform to these La-rich oxides, though their characteristic peaks are not found which may be due to their low content as well as overlapping with other phase peaks. When we enhance the aging temperature up to 1673 K, a more obvious solid state reaction would occur to form the ideal magnetoplumbite-type LaMA phase according to the strict stoichiometry ratio. Since such a solid state reaction can be facilitated at this reduced temperature owing to the presence of MgO.[42] As a result, $MgAl_2O_4$ spinel as the intermediate phase forms during this process. One other indication for the presence of the La-rich intermediate phases is the very weak $LaAlO_3$ and $MgAl_2O_4$ peaks, which do not count for the large remaining mass after the crystallization of single phase LaMA. Besides, as the XRD patterns shown in Fig. 3(g), the relative intensity of another unidentified peak at $2\theta = 26.7°$ increases obviously, this may be the indication of another La-rich intermediate phase between the $LaAlO_3$ phase and the final ideal LaMA phase.

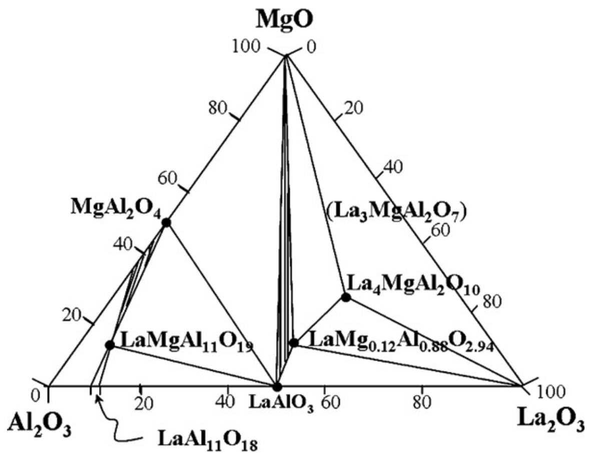

Fig. 4. Phase diagram of ternary system La_2O_3–MgO–Al_2O_3 (in molar percent), after Ref. 30.

3.3. Microstructure

In order to trace the recrystallization process, the fractured cross-sections of the plasma sprayed LaMA coating after aging at different temperatures for 20 h have been examined by SEM, and the micrographs are shown in Fig. 5. A general impression is that the isothermal aging temperatures have strong influences on the rates of the recrystallization and grain growth of the plasma sprayed LaMA coating, resulting in the microstructure evolutions of the LaMA coating very interesting during aging processes. As shown in Fig. 5(a), the as-sprayed LaMA coating displays a large amount of amorphous phase and a low porosity level, which is much similar to the previously reported mullite coating.[6,27] While, the lamellar structure with fine columnar grains located in, as found for other plasma sprayed ceramic coatings, is absent for the present LaMA coating. The rapid cooling which freezes the high temperature phase during plasma spraying process is believed to be tightly correlated to the formation of the amorphous LaMA phase. On the other hand, during plasma spraying, the layered spinel structure with La^{3+}-containing intermediate mirror layers of the LaMA crystal may inhibit the rapid crystallization of the molten LaMA droplets to some extent and cause some contributions to the formation of amorphous phase in the end. After the LaMA coating being thermally aged at 873 K and 1073 K, as the fractured cross-section SEM micrographs shown in Fig. 5(b) and (c), respectively, the layered cleavage characteristics of LaMA coating seems to be more obvious compared with the as-sprayed condition. Layered cleavage is a very common characteristic of the hexaluminate with the magnetoplumbite-type structure, which imparts such kind of oxides with excellent fracture toughness.[34,43] After aging at 1173 K, which is the peak temperature during the recrystallization process as can be seen in the DSC curve in

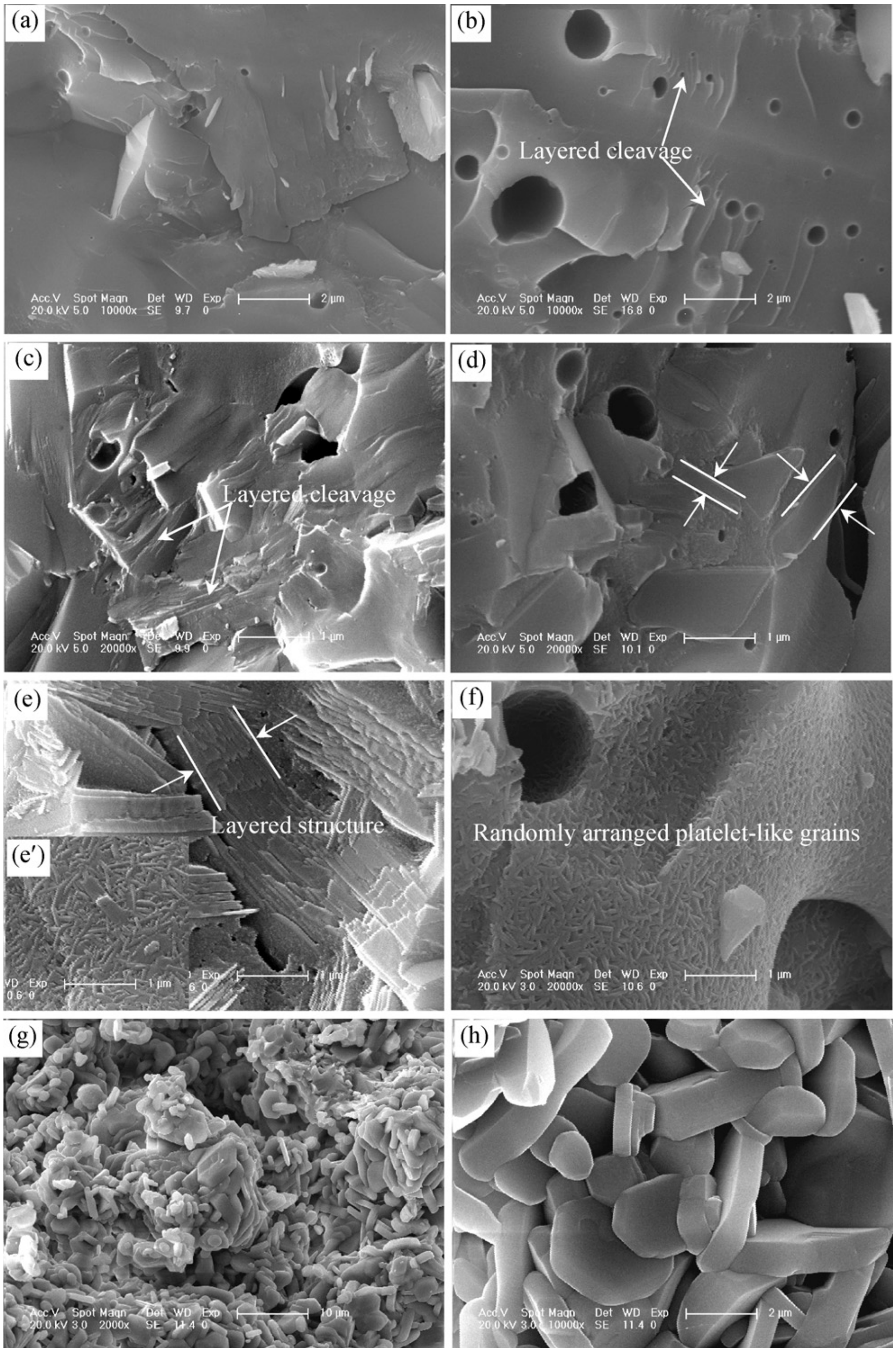

Fig. 5. Fractured cross-section SEM micrographs of LaMA coating: (a) as-sprayed, and after aging for 20 h at 873 K (b), 1073 K (c), 1173 K (d), 1273 K (e) and (e′) selected from different districts, 1473 K (f) and 1673 K (g) and (h) with the different magnifications of 2000× and 10^4×.

Fig. 2, some platelet-like grains as have been marked out in Fig. 5(d), are embedded in the coating matrix. These grains may be induced by the recrystallization, which are much different from the unmelted LaMA particles presented in the fractured cross-section and as well as the coating matrix which is the typical amorphous LaMA phase. As the fractured cross-section SEM micrographs shown in Fig. 5(e) and (e′), it can be observed that the grain growth process has been significantly accelerated and lots of platelet-like grains present consequently when the aging temperature has been enhanced up to 1273 K. Furthermore, it is worth noting that Fig. 5(e) and (e′) displays two different districts characterized by the regularly and irregularly arranged platelet-like grains, respectively. Most of these fine grains with the thickness about 50 nm, and are believed to be recrystallized from the melted splat of the as-sprayed LaMA coating. It can be seen in Fig. 5(e) that the fine platelet-like grains with an average thickness about 30 nm are stacked paralleling to their basal plane. Moreover, it is very interesting to find that such kind of clusters consisting of stacked fine grains (designated as the nanosized sub-grains) as marked by the arrows possess a total thickness about 500–1000 nm which is close to the origin grain thickness of the as-synthesized LaMA powders through a solid state reaction method. Hence, these nanosized sub-grain clusters are likely to be recrystallized from such grains embedded in the coating matrix as marked out in Fig. 5(d). However, the district photographed from the same specimen after aging at 1273 K for 20 h as shown in Fig. 5(e′), displays an irregular arrangement of platelet-like LaMA grains, which is the same to the coating after aging at 1473 K for 20 h as its fractured cross-section SEM micrograph illustrated in Fig. 5(f). The only difference between Fig. 5(e′) and (f) is that the platelet-like grains presented in the later have thickened and coarsened. Therefore, one can assume the plasma spraying and the following aging processes of LaMA coating like this: during plasma spraying, some spherical powders with the particle size distribution between 20 and 120 μm obtained from spray drying underwent different melting condition when they passed through the plasma flame with an extremely high temperature. The surface layer of these spherical powders might be completely melted to produce the droplets. While, by considering the thickness of such spherical powders and as well as the thermal diffusion rate, the temperature grade across the thickness direction of these spherical powders would result in the inner layer with a lower temperature level which might just reach the melting point of LaMA oxide and only intenerate the platelet-like grains, that is to say reaching the critical temperature condition where the transition to the glassy state occurred. When impacting onto the substrate to form the coating together with the melted surface layer, the platelet-like texture of such intenerated grains preserved though a slight glass transition occurred. Such a process may be the key reason responsible for the presences of the platelet-like grains embedded in coating matrix and as well as the cluster consisting of stacked nanosized sub-grains with a layered structure as illustrated in Fig. 5(d) and (e), respectively. While the surface layer of the spherical powder which was fully melted and spread on the substrate produced the coating splat resulting in the amorphous phase with the texture of LaMA grains being completely destroyed. For this amorphous phase, a full crystallization process occurred (designated as recrystallization here) during thermal aging, leading to forming randomly arranged platelet-like grains as illustrated in Fig. 5(e′) and (f). As is well known, the presence of the La^{3+} ion in the intermediate mirror layer of the LaMA unit cell could inhibit the grain growth along [0 0 0 1] direction giving rise to forming a platelet-like LaMA grain with high aspect ratio and anisotropic thermal and mechanical properties.[26] Owing to the growth of LaMA grains will be limited by the presence of neighbor grains which is believed to be the same to the grain's growth characteristic of calcium hexaluminate,[43] thus the final randomly arranged platelet-like grains as presented in Fig. 5(e′) and (f) as well as the parallel array of the fine grains to reach a stable state as the microstructure shown in Fig. 5(e) are present. After the LaMA coating being isothermally aged at 1673 K for 20 h, the amorphous phase and the layered clusters with nanosized sub-grains disappear due to the much higher recrystallization and grain growth rates. As further shown in Fig. 5(g) with a low magnification and (h) with a high magnification, the morphologies and sizes of the platelet-like grains presented in the fractured cross-section of the aged LaMA coating are much the same to the sintered LaMA bulk.

Fig. 6(a) and (b) shows the typical HR-TEM images of the fine particles of the LaMA coating before and after aging at 1673 K for 20 h, respectively. Fig. 6(a) displays that amorphous phase as well as the crystalline phase are present in the as-sprayed LaMA coating, and different lattice orientations can be observed due to the milled LaMA coating particle consisting of the grains with different orientations. After thermal aging, the HR-TEM image shown in Fig. 6(b) exhibits a typical lattice configuration of the hexaluminate with the magnetoplumbite-type structure. It indicates that a transformation of disorder to order has occurred to the as-sprayed LaMA coating during the thermal aging process,

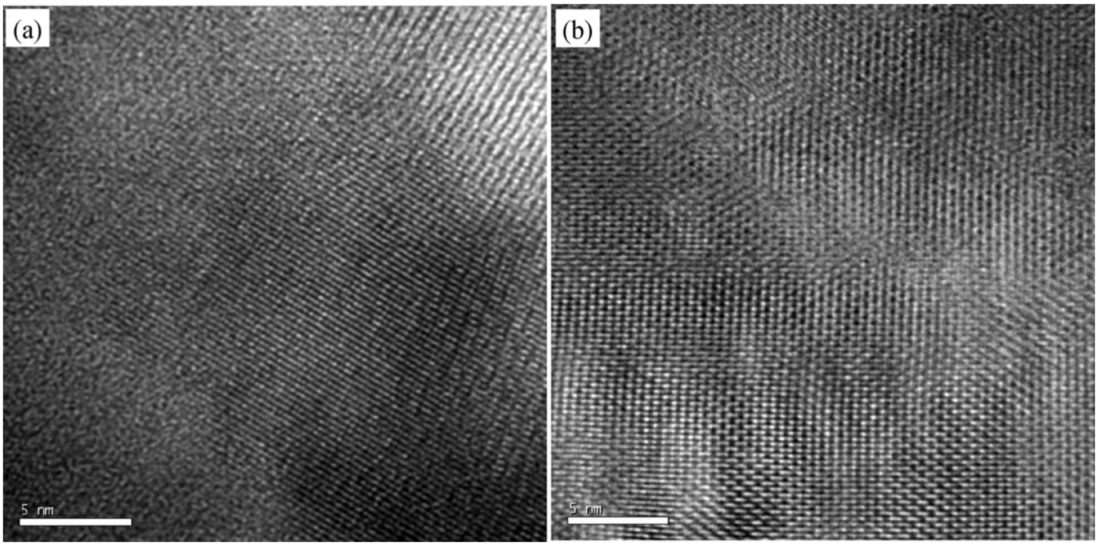

Fig. 6. High-resolution TEM images of the LaMA coating particles: (a) as-sprayed and (b) after aging at 1673 K for 20 h.

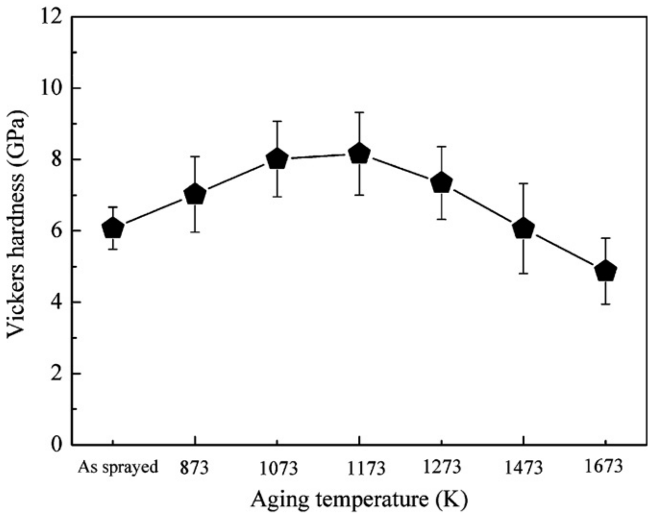

Fig. 7. Vickers microhardness of the as-sprayed LaMA coating and the coating after thermal aging at different temperatures for 20 h.

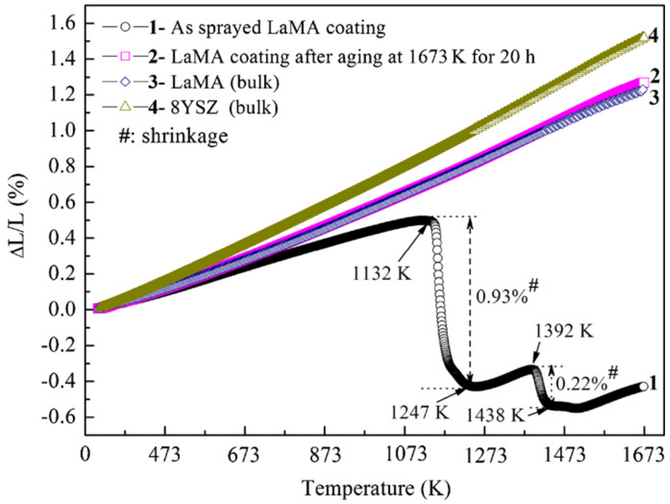

Fig. 8. Linear thermal expansion curves of the LaMA coating before and after thermal aging at 1673 K for 20 h in comparison with the bulks of 8YSZ and LaMA.

resulting in the aged LaMA coating with a perfect crystalline condition.

Fig. 7 shows the Vickers hardness of LaMA coating after aging at different temperatures for 20 h. The Vickers hardness exhibits a nonmonotonic variation under a fixed load. The as-sprayed LaMA coating exhibits a mean Vickers hardness value of 6.07 ± 0.59 GPa. In the present study with a constant aging duration of 20 h, there is a gradual increase in Vickers hardness with the enhancement in aging temperature, and LaMA coating exhibits the highest mean Vickers hardness value of 8.16 ± 1.16 GPa after aging at 1173 K. After that, a more obvious decrease in mean Vickers hardness can be observed with a further increase in the aging temperature. As can be seen in Fig. 7, after aging at 1673 K for 20 h, LaMA coating exhibits a mean Vickers hardness value of 4.87 ± 0.92 GPa which is even lower than that of the as-sprayed coating. It is believed that the variation of the Vickers hardness of LaMA coating during thermal aging processes is tightly correlated to the microstructure evolutions. As the microstructure evolutions schematically shown in Fig. 5, when the aging temperature increases from RT to the peak temperature of recrystallization (∼1173 K as shown in Fig. 2), microcracks and micropores may begin to heal to result in the densification of the ceramic coating and thus an increase in Vickers hardness, though such a process may evolve at a low speed. Besides, with the enhancement in aging temperature, all the well crystallized phases presented in LaMA coating as denoted by the sharpened XRD peaks in Fig. 3, can also cause some contributions to the slight increase in Vickers hardness. As the temperature further increases, faster recrystallization rates and grain growth occur resulting in different microstructures as shown at the fracture cross-section micrographs given in Fig. 5(e) and (e′)–(h). These microstructures yield a gradual increase in porosity levels but reduced Vickers hardness. The reduced Vickers hardness is believed to impart the LaMA coating with an improved strain tolerance and performance in service.

3.4. Thermal expansion behavior

Usually, thermal expansion mismatch between the ceramic top coat and the metallic bond coat would lead to the formations of stresses, which is the key factor responsible for the spallation failure of a TBC system. Therefore, the thermal expansion behavior of the plasma sprayed LaMA coating before and after thermal aging at 1673 K for 20 h have been examined, and their linear expansion curves are compared in Fig. 8. The as-sprayed LaMA coating shows an approximately linear expansion from RT to 1132 K, then it suffers two significant shrinkages of 0.93% and 0.22% ascribed to recrystallization of amorphous LaMA phase and the γ to α-Al_2O_3 phase transition, respectively, which has been pointed in our previous work.[41] The temperature range where shrinkages occur are consistent to the results of thermal analysis as discussed above. After aging at 1673 K for 20 h, as illustrated in Fig. 8, LaMA coating shows a rather similar linear thermal expansion behavior to the sintered LaMA bulk across the entire temperature range, though it is slightly inferior to the typical 8YSZ (8 wt.% yttria stabilized zirconia) bulk. This implies that the completely crystallized LaMA coating possesses the same thermal properties to the sintered LaMA bulk having outstanding thermal shock resistances as pointed in our former work.[44] However, it is worth noting that the as-sprayed LaMA coating exhibits an inferior linear thermal expansion rate to the thermally aged LaMA coating and the sintered LaMA bulk over the temperature range before the first sudden shrinkage occurs. This is another indication of the presence of amorphous phase in the as-sprayed LaMA coating, since the short textured amorphous phase with a large thermal expansion tolerance during heating would result in the as-sprayed LaMA with an inferior macrographic expansion value as the results shown in Fig. 8 and Table 3. The measured average CTEs of the LaMA coating before and after isothermal aging at 1673 K for 20 h as well as the LaMA and 8YSZ bulks are listed in Table 3. Compared with the 8YSZ bulk having a higher average CTE value of $\sim 11.1 \times 10^{-6}\ K^{-1}$, the as-sprayed LaMA coating shows an

Table 3
Measured coefficients of thermal expansion for bulks of 8YSZ, LaMA, and the LaMA coatings before and after aging at 1673 K for 20 h.

Material	Average CTE ($\times 10^{-6}$ K^{-1})
LaMA coating (as-sprayed)	~6.1 (RT to 1113 K)
LaMA coating (after aging)	~9.2 (RT to 1673 K)
LaMA (bulk)	~9.0 (RT to 1673 K)
8YSZ (bulk)	~11.1 (RT to 1673 K)

average CTE value of $\sim 6.1 \times 10^{-6}$ K^{-1} from about 300 K to 1113 K, then, serious contractions resulted from recrystallization and phase transformation upon heating result in such a coating with much lower average CTE value over the entire temperature range. However, the thermally aged LaMA coating exhibits an average CTE value of $\sim 9.2 \times 10^{-6}$ K^{-1} across the temperature range of 300–1673 K, which is close to its bulk counterpart ($\sim 9.0 \times 10^{-6}$ K^{-1}), both of the values agree with the previously published values by Bansal et al.[23] and Friedrich et al.[27] The slight difference in the CTE values between the aged LaMA coating and the sintered bulk may be due to the small differences in their porosity levels. These results indicate that a perfectly crystallized LaMA coating will exhibit improved CTE value compared with the as-sprayed LaMA coating having a large amount of amorphous phase, which will be more preferable to mitigate the thermal expansion mismatch stress level of a LaMA coating-containing TBC system.

4. Conclusion

Atmospheric plasma spraying usually produces a LaMA coating with a large amount of amorphous phase as the typical mullite coating. The recrystallization of the amorphous phase during high temperature service will cause sudden changes in C_p having a strong influence on the thermal conductivity, and as well as in CTE giving rise to the formations of interface residual stresses in a LaMA coating-containing TBC system. The recrystallization and grain growth rates can be significantly accelerated when LaMA coating is isothermally aged at temperature above 1173 K. The well crystallized LaMA coating exhibits improved properties such as reduced microhardness with the consequences of improved strain tolerance and thermal shock resistance, enhanced CTE and C_p close to its bulk counterpart etc. The nanosized LaMA grains and sub-grains are present when the isothermal aging temperature is held between 1273 and 1473 K, and disappear after aging at a higher temperature of 1673 K for a certain duration such as 20 h investigated in the present study. Based on the above results, it seems that a post-deposition annealing of the as-sprayed LaMA coating prior to use at the temperature range of 1173–1273 K is preferable to promote the initial crystallization of amorphous phase. Simultaneously, the rapid recrystallization and the platelet-like LaMA grain growth which will result in a higher stress level and reduced bond strength between the LaMA coating and underlying substrate can be avoided. The present investigation is believed to give useful guidelines to further improve the performances of the LaMA thermal barrier coating as well as other MgO-doped rare earth hexaluminates coatings with the magnetoplumbite-type structure in the future, through the optimization of the processing parameters and adopting other advanced technologies for coating depositions.

Acknowledgements

The authors thank Ms. Meiye Li for the SEM examinations, Mr. Kuiyue Yang for the DSC measurements and Dr. Bilge Saruhan-Brings and Dr. Uwe Schulz (Institute of Materials Research, German Aerospace Center) for the helpful discussions on the results and literature search. The financial supports from the projects of NSFC-50825204, NSFC-20921002 and Lotus Scholars Program of Hunan are also gratefully acknowledged.

References

1. Padture NP, Gell M, Jordan EH. Thermal barrier coatings for gas-turbine engine applications. *Science* 2002;**296**(4):280–4.
2. Clarke DR, Phillpot SR. Thermal barrier coating materials. *Mater Today* 2005;**8**(6):22–9.
3. Rahaman MN, Gross JR, Dutton RE, Wang H. Phase stability, sintering, and thermal conductivity of plasma-sprayed ZrO_2–Gd_2O_3 compositions for potential thermal barrier coating applications. *Acta Mater* 2006;**54**(6):1615–21.
4. Kokini K, DeJonge J, Rangaraj S, Beardsley B. Thermal shock of functionally graded thermal barrier coatings with similar thermal resistance. *Surf Coat Technol* 2002;**154**:223–31.
5. Cao XQ, Vassen R, Stoever D. Ceramic materials for thermal barrier coatings. *J Eur Ceram Soc* 2004;**24**(1):1–10.
6. Girolamo GD, Blasi C, Pilloni L, Schioppa M. Microstructural and thermal properties of plasma sprayed mullite coatings. *Ceram Int* 2010;**36**:1389–95.
7. Xu ZH, He LM, Mu RD, He SM, Huang GH, Cao XQ. Hot corrosion behavior of rare earth zirconates and yttria partially stabilized zirconia thermal barrier coatings. *Surf Coat Technol* 2010;**204**:3652–61.
8. Jones RL. Some aspects of the hot corrosion of thermal barrier coatings. *J Thermal Spray Technol* 1997;**6**:77–84.
9. Leoni M, Jones RL, Scardi P. Phase stability of scandia–yttria-stabilized zirconia TBCs. *Surf Coat Technol* 1998;**108–109**:107–13.
10. Raghavan S, Wang H, Dinwiddie RB, Porter WD, Vassen R, Stöver D, et al. Ta_2O_5/Nb_2O_5 and Y_2O_3 co-doped zirconias for thermal barrier coatings. *J Am Ceram Soc* 2004;**87**:431–7.
11. Liu L, Xu Q, Wang F, Zhang H. Thermophysical properties of complex rare-earth zirconate ceramic for thermal barrier coatings. *J Am Ceram Soc* 2008;**91**:2398–401.
12. Saruhan B, Schulz U, Bartsch M. Developments in processing of ceramic top coats of EB-PVD thermal barrier coatings. *Key Eng Mater* 2007;**333**:137–46.
13. Schulz U, Saruhan B, Fritscher K, Leyens C. Review on advanced EB-PVD ceramic topcoats for TBC applications. *Int J Appl Ceram Technol* 2004;**1**(4):302–15.
14. Vassen R, Traeger F, Stöver D. New thermal barrier coatings based on pyrochlore/YSZ double-layer systems. *Int J Appl Ceram Technol* 2004;**1**:351–61.
15. Vassen R, Cao X, Tietz F, Basu D, Stöver D. Zirconates as new materials for thermal barrier coatings. *J Am Ceram Soc* 2000;**83**:2023–8.
16. Liu ZG, Ouyang JH, Zhou Y, Li J, Xia XL. Influence of ytterbium- and samarium-oxides codoping on structure and thermal conductivity of zirconate ceramics. *J Eur Ceram Soc* 2009;**29**(4):647–52.
17. Liu ZG, Ouyang JH, Zhou Y, Li J, Xia XL. Densification, structure and thermophysical properties of ytterbium-gadolinium zirconate ceramics. *Int J Appl Ceram Technol* 2009;**6**(4):485–91.
18. Liu ZG, Ouyang JH, Zhou Y, Xia XL. Hot corrosion behavior of V_2O_5-coated $Gd_2Zr_2O_7$ ceramic in air at 700–850 °C. *J Eur Ceram Soc* 2009;**29**(11):2423–7.

19. Cao XQ, Vassen R, Tietz F, Stöver D. Lanthanum–cerium oxide as a thermal barrier-coating material for high-temperature applications. *Adv Mater* 2003;**15**:1438–42.
20. Dai H, Zhong XH, Li JY, Meng J, Cao XQ. Neodymium–cerium oxide as new thermal barrier coating material. *Surf Coat Technol* 2006;**201**:2527–33.
21. Ma W, Mack DE, Vassen R. Perovskite-type strontium zirconate as a new material for thermal barrier coatings. *J Am Ceram Soc* 2008;**91**(8):2630–5.
22. Choi SR, Bansal NP, Zhu DM. Mechanical and thermal properties of advanced oxide materials for higher-temperature coatings applications. *Ceram Eng Sci Proc* 2005;**26**(3):1–9.
23. Bansal NP, Zhu DM. Thermal properties of oxides with magnetoplumbite structure for advanced thermal barrier coatings. *Surf Coat Technol* 2008;**202**(12):2698–703.
24. Pracht G, Vassen R, Stöver D. Lanthanum–lithium hexaaluminate – a new material for thermal barrier coatings in magnetoplumbite structure-material and process development. *Ceram Eng Sci Proc* 2007;**27**(3):87–99.
25. Vassen R, Jarligo MO, Steinke T, Mack DE, Stöver D. Overview on advanced thermal barrier coatings. *Surf Coat Technol* 2010;**205**:938–42.
26. Gadow R, Lischka M. Lanthanum hexaaluminate – novel thermal barrier coatings for gas turbine applications – materials and process development. *Surf Coat Technol* 2002;**151/152**:392–9.
27. Friedrich C, Gadow R, Schimer T. Lanthanum hexaaluminate – a new material for atmospheric plasma spraying of advanced thermal barrier coatings. *J Therm Spray Technol* 2001;**10**(4):592–8.
28. Schaefer GW, Gadow R. Lanthanum aluminate thermal barrier coating. *Ceram Eng Sci Proc* 1999;**20**(4):291–7.
29. Friedrich C, Gadow R, Lischka MH. Lanthanum hexaaluminate thermal barrier coatings. *Ceram Eng Sci Proc* 2001;**22**(4):375–82.
30. Gadow R, Schaefer G. *Thermal insulating material and method of producing same*. US Patent No. 6,998,064; 2006.
31. Cao XQ, Zhang YF, Zhang JF, Zhong XH, Wang Y, Ma HM, et al. Failure of the plasma-sprayed coating of lanthanum hexaluminate. *J Eur Ceram Soc* 2008;**28**(10):1979–86.
32. Chen XL, Zhang YF, Zhong XH, Xu ZH, Zhang JF, Cheng YL, et al. Thermal cycling behaviors of the plasma sprayed thermal barrier coatings of hexaluminates with magnetoplumbite structure. *J Eur Ceram Soc* 2010;**30**:1649–57.
33. Saruhan-Brings B, Schulz U, Kroder CJ. *Thermal-insulating material having an essentially magnetoplumbitic crystal structure*. US Patent No. 2006/0019107; 2006.
34. Kahn A, Lejus AM, Madsac M, Thery J, Vivien D. Preparation, structure, optical, and magnetic properties of lanthanide aluminate single crystals ($LnMAl_{11}O_{19}$). *J Appl Phys* 1981;**52**(11):6864–9.
35. Coltongues R, Gourier D, Kahn-Harari A, Lejus AM, Théry J, Vivien D. Magnetoplumbite-related oxides. *Annu Rev Mater Sci* 1990;**20**:51–82.
36. Cinibulk MK. Thermal stability of some hexaluminates at 1400 °C. *J Mater Sci Lett* 1995;**14**:651–4.
37. Jiang B, Fang MH, Huang ZH, Liu YG, Peng P, Zhang J. Mechanical and thermal properties of $LaMgAl_{11}O_{19}$. *Mater Res Bull* 2010;**45**:1506–8.
38. Anderson OL. A simplified method for calculating the debye temperature from elastic constants. *J Phys Chem Solids* 1963;**24**:909–18.
39. Schreiber E, Aderson OL, Soga N. *Elastic Constants and their Measurement*. New York, USA: McGraw-Hill; 1973.
40. Ding XZ, Liu XH. The Debye temperature of nanocrystalline titania measured by two different methods. *Phys Stat Sol (a)* 1996;**158**:433–9.
41. Chen XL, Zhao Y, Fan XZ, Liu YJ, Zou BL, Wang Y, et al. Thermal cycling failure of new $LaMgAl_{11}O_{19}$/YSZ double ceramic top coat thermal barrier coating systems. *Surf Coat Technol* 2010;**205**:3293–300.
42. Cinibulk MK. Effect of divalent cations on the synthesis of citrate-gel-derived lanthanum hexaluminate powders and films. *J Mater Res* 1999;**14**:3581–93.
43. Domínguez C, Chevalier J, Torrecillas R, Gremillard L, Fantozzi G. Thermomechanical properties and fracture mechanisms of calcium hexaluminate. *J Eur Ceram Soc* 2001;**21**:907–17.
44. Zhang JF, Zhong XH, Cheng YL, Wang Y, Xu ZH, Chen XL, et al. Thermal-shock resistance of $LnMgAl_{11}O_{19}$ (Ln = La, Nd, Sm, and Gd) with magnetoplumbite structure. *J Alloys Compd* 2009;**482**(1–2):376–81.